JACS Au
AN OPEN ACCESS JOURNAL OF THE AMERICAN CHEMICAL SOCIETY

pubs.acs.org/jacsau
Letter

Phosphorus-Doped Multilayer In_6Se_7: The Study of Structural, Electrical, and Optical Properties for Junction Device

Yu-Hung Peng, Luthviyah Choirotul Muhimmah, and Ching-Hwa Ho*

Cite This: *JACS Au* 2024, 4, 58−71

Read Online

ACCESS | Metrics & More | Article Recommendations | Supporting Information

ABSTRACT: This work investigates the characteristic of layered In_6Se_7 with varying phosphorus (P) dopant concentrations (In_6Se_7:P) from P = 0, 0.5, 1, to P = 5%. X-ray diffraction (XRD) and transmission electron microscopy (TEM) analyses indicate that the structure and morphology of the In_6Se_7:P series compounds remain unchanged, exhibiting a monoclinic structure. Room-temperature micro-Raman (μRaman) result of all the compositions of layered In_6Se_7:P reveals two dominant peaks at 101 ± 3 cm^{-1} (i.e., In−In bonding mode) and 201 ± 3 cm^{-1} (i.e., Se−Se bonding mode) for each P composition in In_6Se_7. An extra peak at approximately 171 ± 2 cm^{-1} is observed and it shows enhancement at the highest P composition of In_6Se_7:P 5%. This mode is attributed to P−Se bonding caused by P doping inside In_6Se_7. All the doped and undoped In_6Se_7:P showed *n*-type conductivity, and their carrier concentrations increased with the P dopant is increased. Temperature-dependent resistivity revealed a reduction in activation energy (for the donor), as the P content is increased in the In_6Se_7:P samples. Kelvin probe measurement shows a decrease in work function (i.e., an energy increase of Fermi level) of the *n*-type In_6Se_7 multilayers with the increase of P content. The indirect and direct band gaps for all of the multilayer In_6Se_7:P of different P composition are identical. They are determined to be 0.732 eV (indirect) and 0.772 eV (direct) obtained by microtransmittance and microthermoreflectance (μTR) measurements. A rectified n−n^+ homojunction was formed by stacking multilayered In_6Se_7/In_6Se_7:P 5%. The built-in potential is about V_{bi} ∼ 0.15 V. It agrees well with the work function difference between the two layer compounds.

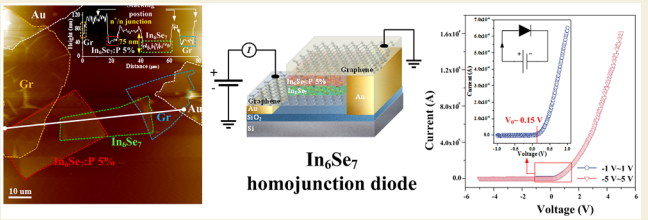

KEYWORDS: *In_6Se_7, energy compound, n-type semiconductor, P−Se bond, band gap*

1. INTRODUCTION

III−VI layered semiconductors have gained significant attention due to their unique electronic and optical properties as well as specific technological applications.[1,2] The III and VI monochalcogenides possess a general chemical formula of MX, where M is a group III element (such as Ga or In), and X is a chalcogen atom (such as Te, Se, or S).[3−6] One of the most exciting properties of III−VI layered semiconductors is their direct band edge constructed in the multilayer form,[7−9] this can make them an ideal candidate for various optoelectronics applications such as solar cells, photodetectors, and light-emitting diodes.[10−15] Indium is easily oxidized and exhibits intriguing characteristics within the group III elements, especially as it forms many compounds by synthesis with group VI elements, such as In−O,[16,17] In−S,[18−21] In−Se,[22−24] and In−Te.[25,26] The formation of In−Se bonding is important in III−VI compounds, and it has been extensively studied and investigated for its derivatives in various applications.[9,11,27−29] The investigation of In−Se-based materials is driven by their potential utilization in various applications, including solar cells,[30,31] Li-ion batteries,[32−34] and ionizing radiation detectors,[35] due to their noteworthy physical features, such as optical and electrical properties.[36] The materials of the In−Se system have also attracted considerable interest due to its intrinsic structural properties, including phase transition (transformation), multicrystalline zones consisting different phases, and structural imperfections.[37,38] Extensive research has been conducted on materials derived from the In−Se system,[39−42] and numerous works have investigated the phase diagram of the In−Se system with different stoichiometry and different modifications.[43−45] Previous investigations have reported that the presence of stable phases in this In−Se system includes the stoichiometric compositions of InSe,[43] In_2Se_3,[46] In_4Se_3,[47] and In_6Se_7.[36,48] Nevertheless, certain characteristics of this specific In_xSe_y system have not yet been systematically examined to date.

Among the III−VI compounds, In_6Se_7 holds significant importance and it attracts a lot of scientific interests on structure study due to its crystallization is in $P2_1/m$ space

Received: October 24, 2023
Revised: November 24, 2023
Accepted: November 27, 2023
Published: November 30, 2023

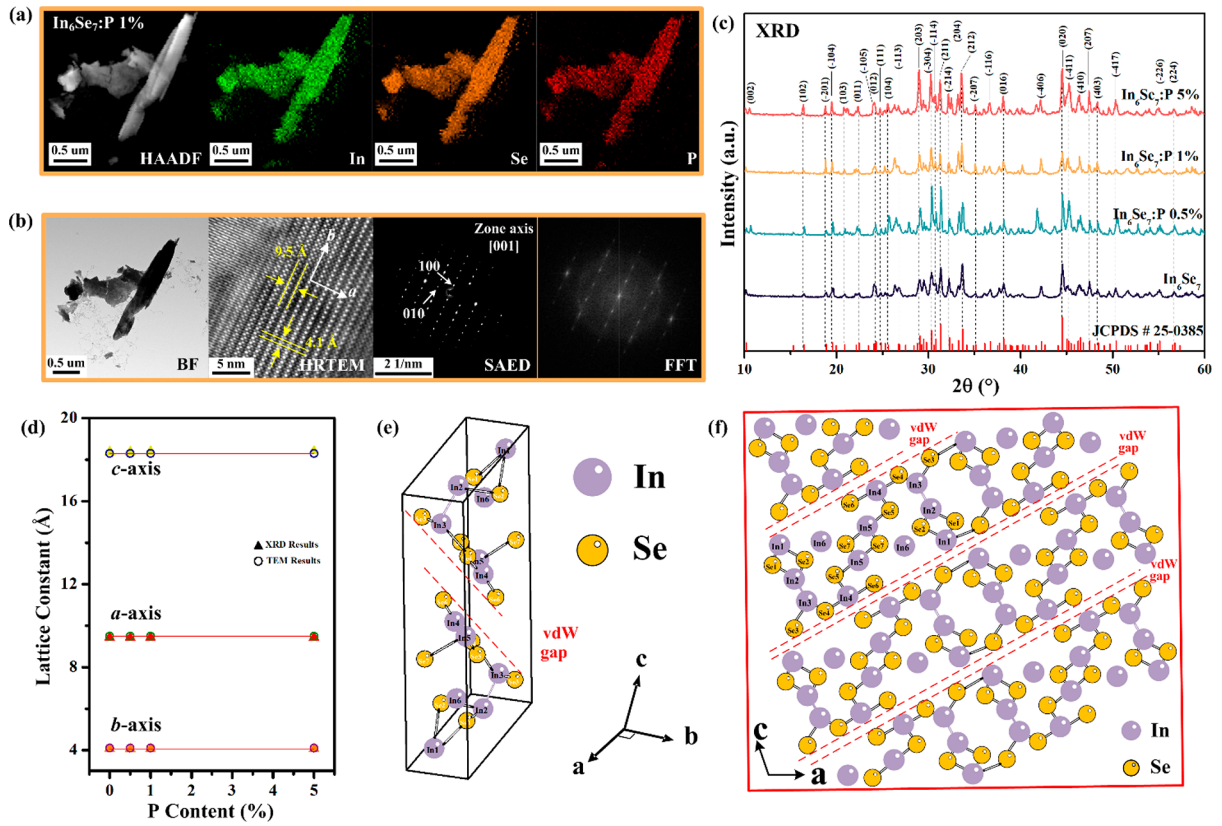

Figure 1. Study of crystal structure, crystal quality and stoichiometry of In_6Se_7:P. (a) HAADF-STEM image of elements (In, Se, and P) in representative sample of In_6Se_7:P 1% nanoflake. (b) Bright-field (BF) images from TEM result, high-resolution (HR) TEM images, SAED pattern, and corresponding FFT diffractions of the In_6Se_7:P 1% sample. (c) Powdered X-ray diffraction patterns of In_6Se_7:P (P = 0%, 0.5%, 1%, and 5%) series compounds in the 2θ angle range of 10°−60° at 300 K. (d) Lattice constants determined by XRD and TEM measurement dependent on P content. (e) The three-dimensional side view of the atomic model of In_6Se_7. (f) Two-dimensional side view of the atomic arrangement of In_6Se_7.

group of monoclinic structure.[49−51] The unique characteristic sets it apart from other materials in the In−Se system, e.g., InSe and In_2Se_3, which typically exhibited a hexagonal structure.[43,46] However, further investigation is required to examine the correlation between its attributes and special properties, such as optical and electrical characterization. The comprehensive analysis of this In_6Se_7 compound is limited because of the difficulties in growing large single crystals of this material. There is a lack of extensive research on the thermoelectric, conductivity, band gap, electronic, and optical properties of In_6Se_7. Despite the significance of gaining insight into the molecular structure, there is a dearth of early theoretical and experimental studies for examining the characteristics of In_6Se_7.[36,48] The low band gap of In_6Se_7 (<0.9 eV) may enhance its ability to capture electrons with energy levels corresponding to the near-infrared (NIR)-visible light, and makes it an attractive material for photon absorption and utilization in various devices. The advantageous energy level could also improve photon-absorption efficiency in photovoltaics, where In_6Se_7 can play a potential material for absorption of a wider spectrum of solar energy.

In this work, crystal growth and characterization of the P doped In_6Se_7 from P = 0, 0.5, 1 and 5% content are reported. The influence of P doping on the electrical, electronic, optical, and structural properties of the multilayered In_6Se_7 is detailed examined. Undoped In_6Se_7 is intrinsically categorized as an *n*-type semiconductor.[48] In order to improve the carrier-transport behavior, a definite amount of phosphorus (P) dopant is introduced into the pure In_6Se_7 material. The phosphorus doping does not change the carrier type from *n* to *p* but employs to enhance the number of electrons that present in the In_6Se_7 crystal. The work involves the growth of single crystals belonging to the In_6Se_7:P (P = 0%, 0.5%, 1%, 5%) series by utilizing the chemical vapor transport (CVT) method with ICl_3 as the transport agent. The X-ray diffraction (XRD) investigation on this series confirms the isostructural characteristic of the In_6Se_7:P series compounds. The compounds are found to crystallize in the monoclinic structure of $P2_1/m$ symmetry. The lattice constants and crystal structure of the In_6Se_7:P series compounds exhibit no discernible differences. The micro-Raman (μRaman) measurements indicate that In_6Se_7:P series compounds exhibit similar vibrational modes at the same frequencies except a widened Raman peak appears as the P-doping level is increased. Hall-effect and hot probe measurements reveal *n*-type conductivity for the whole series In_6Se_7:P (P = 0%, 0.5%, 1%, 5%) and the carrier density of the semiconductor increases as the P concentration increases. Temperature-dependent resistivity measurements were performed to investigate the electrical characteristics of In_6Se_7:P as a function of temperature. The decrease of electron activation energy (ΔE) with the increase of the P dopant leads the increase of electron density. This result is further supported by X-ray photoelectron spectroscopy (XPS) to characterize the electronic peaks linked to selenium (Se) and phosphorus (P). The occurrence of *n*-type conductivity is due to the formation of the P−Se bonds within the In_6Se_7:P crystals.

https://doi.org/10.1021/jacsau.3c00653
JACS Au 2024, 4, 58−71

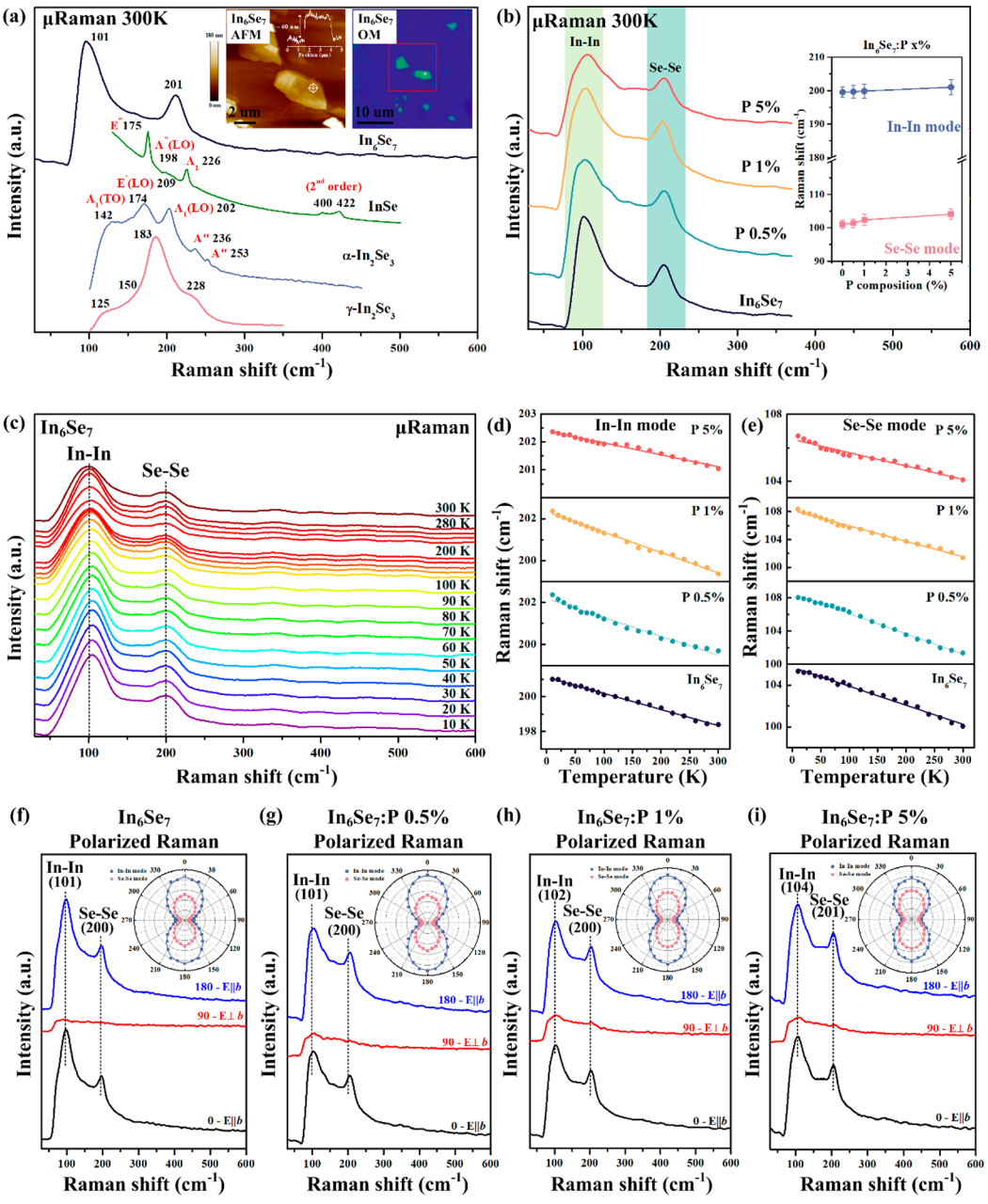

Figure 2. Structure characterization of In_6Se_7:P by μRaman measurement. (a) μRaman spectra of In_6Se_7, InSe, α-In_2Se_3, and γ-In_2Se_3. The inset images show the AFM and OM images of the nanoflake In_6Se_7 sample used for μRaman measurement. (b) μRaman spectra of In_6Se_7:P (P = 0%, 0.5%, 1%, and 5%) series compounds. (c) Temperature-dependent μRaman spectra of a selective sample of In_6Se_7. The linear fit of temperature-energy shift of the In_6Se_7:P series compounds for (d) In−In bonding mode and (e) Se−Se bonding mode from 10 to 300 K. Polarized Raman spectra of In_6Se_7:P series of (f) P 0%, (g) P 0.5%, (h) P 1%, and (i) 5%. The inset images are the polar plot for each P content in (f)−(i).

For the characterization of experimental band structure, a Kelvin probe with mapping function was employed to evaluate the Fermi level and work function uniformity from the multilayered surface of the In_6Se_7:P series compounds. As the P composition increases, the work function of the multilayer In_6Se_7:P series compound is decreased, which associates with the up displacement of the Fermi level toward the conduction band and also sustains a rise of electron density. For further characterization of optical band gaps, microthermoreflectance (μTR) and microtransmittance (μtr) measurements are respectively carried out to assess the direct and indirect band gaps of the multilayered In_6Se_7 from 20 to 300 K. In_6Se_7 exhibits a notable benefit as compared to its III−VI counterpart of multilayer InSe (i.e., direct gap $E_g \sim 1.24$ eV) which shows an indirect band gap of 0.732 eV and a direct gap of 0.772 eV that constructed in its band structure (i.e., below 1 eV) for absorbing more NIR photons under sunlight illumination. The fabrication of an n/n^+ homojunction by stacking the multilayer In_6Se_7:P 5% on pure In_6Se_7 was performed. A diode rectified voltage−current (V−I) curve with a built-in potential of about 0.15 V was obtained. The built-in voltage agrees well with the work function difference between the In_6Se_7:P 5% and pure In_6Se_7 measured by a Kelvin probe. The van der Waals (vdW) stacked diode makes In_6Se_7 a promising candidate for further development as a photovoltaic

https://doi.org/10.1021/jacsau.3c00653
JACS Au 2024, 4, 58−71

device capable of converting NIR to visible sunlight into electric power.

2. RESULTS AND DISCUSSION

For the In_6Se_7 compound, whether the stoichiometric ratio of In:Se is 6:7 is important for the as-grown layer crystals (i.e., make sure the stoichiometry is in distinction to those of the other phases of In_2Se_3 or InSe, *etc.*). Figure 1a shows energy dispersive X-ray spectroscopy (EDS) mapping for a nanoflake In_6Se_7:P 1% as the representative sample from high-resolution electron microscopy (HRTEM). The crystal morphology of the In_6Se_7:P series compound is multiline-edge-like with a silver-shiny color, as shown in Figure S1a. The length of each crystal is approximately 100 μm to 10 mm. All the EDS spectra of the In_6Se_7:P series compounds are shown in Figure S1b−e in the Supporting Information (SI). EDS spectra and mapping results of the In_6Se_7:P series compounds were conducted through high-angle annular dark-field imaging (HAADF) in the scanning transmission electron microscopy (STEM) mode of a FEI Tecnai G2 F-20 S-TWIN TEM/EDS system. From the EDS analyses, the composition of each component in the In_6Se_7:P series is close to the nominal value and the homogeneous mapping composition indicates that the as-grown crystals possess a good quality. The values of EDS analyses for In_6Se_7:P are tabulated in Table S1 in the Supporting Information. Furthermore, EDS mapping through the STEM mode for the In_6Se_7:P series compounds can be seen in Figure S2a−c. The EDS mapping result reveals clear evidence of the uniformity inherent in the In_6Se_7:P series compounds. This observation holds particular significance within the realm of materials science and also emphasizes the consistent and homogeneous distribution of properties that can be observed in the examined multilayer samples.

The HRTEM and selection-area electron diffraction (SAED) results of a representative In_6Se_7:P 1% nanoflake are depicted in Figure 1b. The HRTEM and SAED images clearly indicate the atomic arrangement and axial orientation and also identify the interatomic distance (d-spacing) in In_6Se_7:P 1%, which confirms the monoclinic structure. The dotted spots in the fast Fourier transform (FFT) and SAED patterns of In_6Se_7:P 1% also reveal an indication of a high-quality single crystal. The other HRTEM results for the In_6Se_7:P series compounds are presented in Figure S2d−f. These results verify that the In_6Se_7:P series compounds have a monoclinic structure with a longer crystal edge along the b-axis direction. The values of the lattice constant of the a and b axes are about 9.5 and 4.1 Å observed from HRTEM. Figure 1c shows the XRD pattern for the In_6Se_7:P series (P = 0%, 0.5%, 1%, and 5%) at 300 K with a 2θ range from 0° to 60°. The XRD result reveals that In_6Se_7:P series compounds exhibit a comparable and similar peak feature, with the major peak indices matching the JCPDS 25-0385 reference pattern, as depicted by the red lines at the bottom of Figure 1c. From the comparison of the JCPDS reference pattern and the experimental XRD results of the In_6Se_7:P series (P = 0%, 0.5%, 1%, and 5%), the phosphorus doping may not significantly influence the dominant monoclinic structure of the pure In_6Se_7 compound. The lattice constants of the In_6Se_7:P series can be calculated from the XRD patterns and compared with the d-spacing estimated by the HRTEM and SAED patterns. The obtained values are given in Table S2. Essentially, the lattice constants of the a and b axes are comparable for the In_6Se_7 doped with different P content. All the values of the lattice constants in the monoclinic In_6Se_7:P series (P = 0%, 0.5%, 1%, and 5%) calculated from the XRD patterns in Figure 1c are listed in Table S3 for comparison. Within standard errors, the lattice constants of the P-doped In_6Se_7 series are comparable and are in agreement with the previous JCPDS result of In_6Se_7. The plots of lattice constants that are determined by XRD and TEM results are comparable and presented in Figure 1d. The obtained lattice constants are a = 9.433 ± 0.06 Å, b = 4.068 ± 0.05 Å, c = 18.378 ± 0.05 Å, and β = 109.29° ± 0.05°, respectively. The other doped 2D materials like Cr-doped ReS_2[52] and Cr-doped $ReSe_2$[53] also showed identical structures and unchanged lattice parameters with altered dopant content in the crystals. The Cr in $ReSe_2$ may act as an impurity dopant for changing the carrier concentration of the layer semiconductor.[53] Thus, different P-doped compositions in In_6Se_7 may also be inferred to have an effect on modulation of the carrier density of the layer compounds. The illustration of the structural arrangement is shown in Figure 1e and f where the van der Waals gap is shown. According to prior studies[39,50,51] as well as from the crystal morphology, In_6Se_7:P has a monoclinic structure with a multiline long-edge outline along the b axis. Similar to the other monoclinic structures in the III−VI semiconductors, such as GaTe[8,54] and M-$GaTe_{1-x}Se_x$,[6] the multiline edges are elongated in the $b(y)$ axis.

Figure 2a shows the Raman spectra of In_6Se_7 and previously reported In−Se system materials, specifically γ-In_2Se_3, α-In_2Se_3, and InSe at 300 K. The vibrational spectrum of γ-In_2Se_3 exhibits four modes at 125, 150, 183, and 228 cm^{-1}.[22] α-In_2Se_3 exhibits five peaks observed at 142 cm^{-1}, A_1(TO) 174 cm^{-1}, A_1 (LO) 202 cm^{-1}, A″ 236 and 253 cm^{-1}.[24] Furthermore, InSe indicates five modes of E″ at 175 cm^{-1}, A″ (LO) at 198 cm^{-1}, E′ (LO) at 209 cm^{-1}, A_1 at 226 cm^{-1}, and second order at 400 and 422 cm^{-1}.[11] In contrast, the μRaman spectrum of the thin-layer In_6Se_7 reveals only two peaks positioned at about 101 and 201 cm^{-1}. The inset images in Figure 2a display the atomic force microscopy (AFM) results along with the optical microscopy (OM) picture of the multilayer In_6Se_7. It can serve as a representative illustration for the In_6Se_7:P series of samples with a thickness of about 60 nm. The other In_6Se_7:P compounds were also measured and maintained at a thickness level of below 70 nm. Figure 2b depicts the μRaman spectra of the In_6Se_7:P series compounds (P = 0%, 0.5%, 1% and 5%) at room temperature. The inset image in Figure 2b reveals the plot of Raman frequencies dependent on the P content. The values of the Raman frequencies of In−In and Se−Se modes seem to be comparable within standard errors for the different P-doped In_6Se_7 compounds. Moreover, there is no obvious extra peak observed by the P incorporation in In_6Se_7 at 300 K. The Raman peak feature and morphology of layered In_6Se_7 closely resemble with those of the monoclinic In_6S_7,[55] but it shows a lower vibration frequency due to the heavier atomic mass of selenium (Se) as compared to the sulfur (S) atom. A previous study reported that the peak observed at ∼100 ± 3 cm^{-1} is attributed to In−In vibrations.[56] However, the heavier In element as compared to Se is responsible for the emergence of the higher-frequency peak at ∼202 ± 3 cm^{-1}, which is associated with the Se−Se vibrations.

Figure 2c presents the temperature-dependent Raman spectra of a representative sample In_6Se_7 to show the influence of temperature on lattice vibrations across the temperature range from 10 to 300 K. The Raman spectrum at 10 K demonstrates a significant increase in intensity, along with a reduction in its line width and the blue-shift of peak

https://doi.org/10.1021/jacsau.3c00653
JACS Au 2024, 4, 58−71

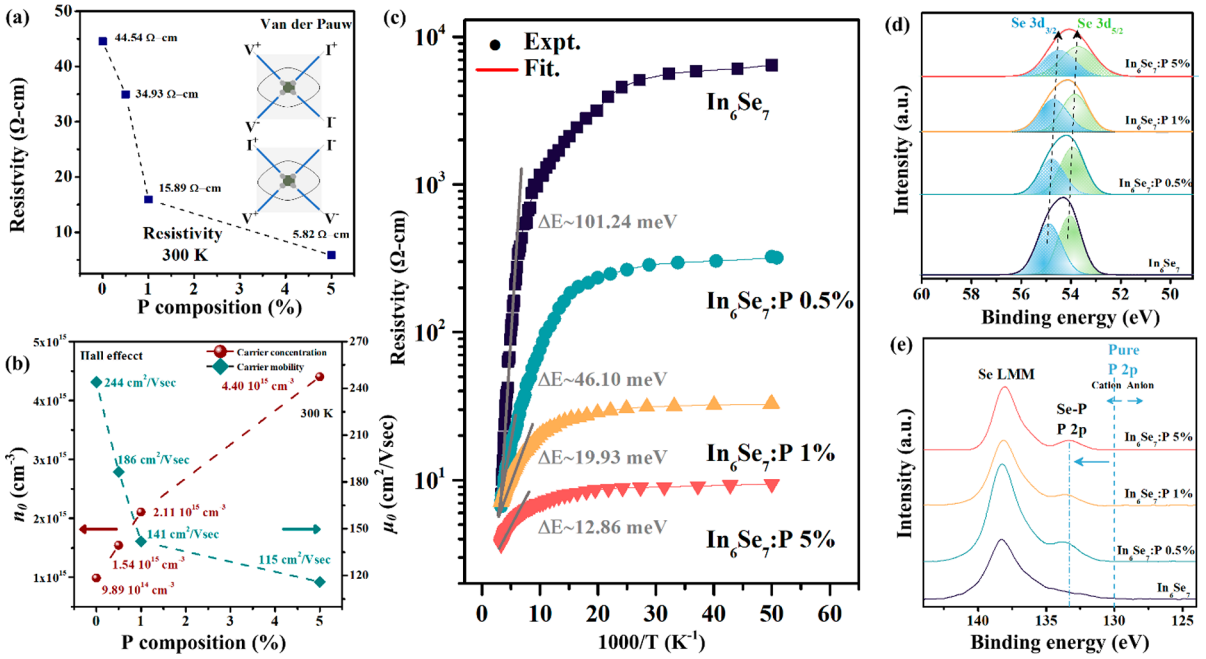

Figure 3. Carrier transport and P-incorporation effect on In_6Se_7:P series compounds. (a) Resistivity versus P composition for In_6Se_7:P (P = 0%, 0.5%, 1%, and 5%) at 300 K. The inset image is the van der Pauw experimental setup illustration. (b) Carrier concentration and carrier mobility versus P composition obtained by Hall-effect measurement of In_6Se_7:P series at 300 K. (c) Temperature-dependent resistivity of In_6Se_7:P series compounds from 20 to 300 K to analyze the activation energy of electrons. XPS spectral analysis of (d) Se 3d and (e) P 2p states of the P-doped In_6Se_7 series compounds.

wavenumber. The temperature-dependent Raman spectra of a representative multilayer In_6Se_7:P 0.5% are illustrated in Figure S3a. The spectral analysis indicates that the peaks observed at 101 and 201 cm^{-1} (300 K) shift toward higher wavenumber, and the line width becomes reduced as the temperature decreases. In Figure S3b, the spectrum obtained at 10 K indicates a prominent peak at 171 cm^{-1}, which maybe associates with the P−Se bonding.[57] Figures S3c present a comparative analysis of the spectra obtained for the In_6Se_7:P series at 10 K. The Raman spectra of In_6Se_7:P (P = 0.5%, 1%, and 5%) at 10 K exhibit a peak at ∼171 ± 2 cm^{-1}. As the P concentration increases, the peak at ∼171 ± 2 cm^{-1} (P−Se bending mode) becomes stronger and more apparent (i.e., as highlight yellow). The frequency change in lattice vibration at different temperatures can be attributed to the alteration in crystal bond length as the temperature changes. The values of the Raman frequencies of the modes are listed in Table S4. The Raman vibrational mode transition as the temperature increases can be analyzed through Vegard's law, a linear relationship with the formula $V(T) = V(0) - m{\cdot}T$, where $V(0)$ is the Raman frequency at 0 K, m is the linear term for this Vegard-like variation, and T is the temperature in Kelvin. The Raman vibrational frequencies of the In−In mode, Se−Se mode, and P−Se mode of In_6Se_7:P (0%, 0.5%, 1%, and 5%) are depicted in Figures 2d,e and S3d. The linear fitting parameters through Vegard's law are listed in Table S5 for comparison. The results indicate an energy reduction in the wavenumbers for the In−In bonding mode, Se−Se bonding mode, and P−Se bonding mode from 10 to 300 K. The observed behavior can be attributed to the phenomenon of lattice expansion in the In_6Se_7:P crystals with leading to a reduction of vibrational frequency. To assess the in-plane structural and optical anisotropy of the In_6Se_7:P series, angular-dependent polarized Raman measurements were conducted. Polarized μRaman measurements covered the angle range of θ = 0−360°, with representative spectra of typical angles of 0° [denoted as light (E) parallel to the b-axis (E∥b)], 90° [E⊥b], and 180° [E∥b]. Figure 2f−i presents the polarized Raman spectra for some selected angles (0°, 90°, and 180°) in the In_6Se_7:P series. The prominent peaks of the In−In mode and Se−Se mode in each P-doped composition exhibit intensity degradation from 0° to 90°. Notably, the peaks at 90° are not strictly forbidden, suggesting that the In_6Se_7:P series demonstrates a predominant symmetry orientation along the b axis.

Figure 3a and b, respectively, illustrates the plots of resistivity from van der Pauw measurement and carrier-transport properties (carrier concentration and mobility) from Hall effect measurements for bulk In_6Se_7:P (P = 0%, 0.5%, 1%, and 5%) samples at 300 K. The inset images of Figure 3a show the experimental setup for the In_6Se_7:P samples used in van der Pauw measurements. Hall-effect and hot-probe measurements showed that the In_6Se_7:P series of compounds demonstrate an n-type conductivity. The Seebeck coefficient measured by hot-probe measurement is given in Table S6. The values of resistivity of the P-doped In_6Se_7 series are shown to be 44.54 Ω·cm for undoped In_6Se_7, 34.93 Ω·cm for P = 0.5%, 15.89 Ω·cm for P = 1%, and 5.82 Ω·cm for P = 5%. As shown in Figure 3b, the carrier concentration increases from 9.88 × 10^{14} cm^{-3} (P 0%) to 4.40 × 10^{15} cm^{-3} (P 5%). However, the carrier mobility values are inversly proportional to the carrier concentration values, which decrease from 244 cm^2/V s (P 0%) to 115 cm^2/V s (P 5%). The higher P-dopant amount results in larger values of conductivity and electron concentration. This result suggests that the phosphorus (P) atom might act as a shallow donor impurity that positioned slightly below the conduction band edge (E_c) within the band gap of In_6Se_7. The observed behavior can be compared to the function of the Cr (Cr^{3+}) dopant in layered rhenium

https://doi.org/10.1021/jacsau.3c00653
JACS Au 2024, 4, 58−71

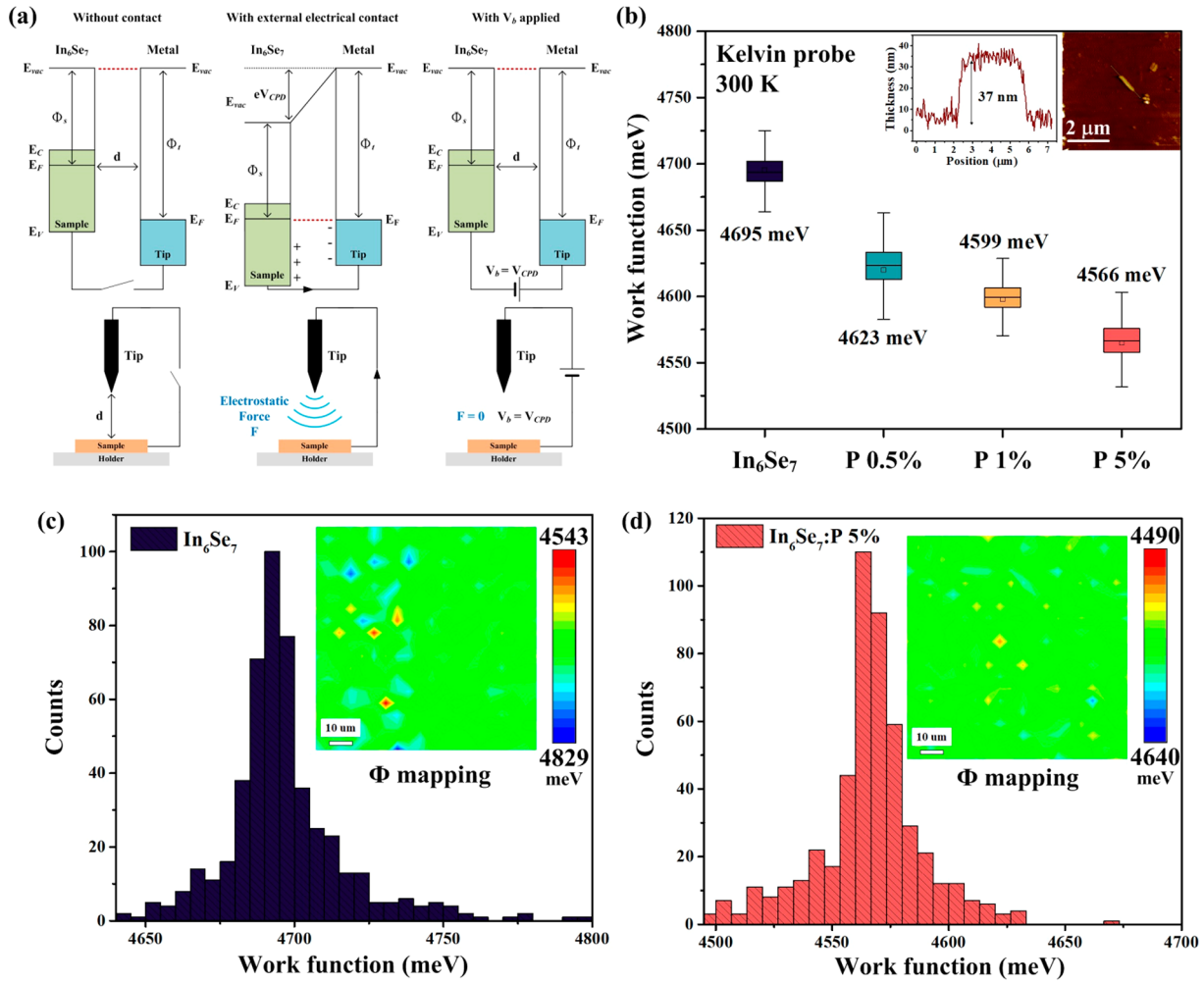

Figure 4. (a) Scheme of Kelvin probe measurement for determining contact potential difference (CPD). (b) Plot of work function determined by each composition of the In_6Se_7:P multilayers at 300 K. The inset image is the AFM result for multilayer In_6Se_7:P 5% as the representative. Work function distribution histogram and 2D mapping plot of (c) bulk In_6Se_7 and (d) bulk In_6Se_7:P 5% within a scanned area of 100 × 100 μm^2 at 300 K.

diselenide, which performs like a shallow acceptor positioned above the valence band edge (E_v) within the band gap of $ReSe_2$.[54]

Two-point photovoltage−current (photo $V-I$) measurements were also carried out to determine photoresponse of In_6Se_7:P, as presented in Figure S4a−d. The measurement conditions are dark condition, illuminated with tungsten halogen lamp (THL), and illuminated with white light-emitting diode (LED), respectively. The optical-power density of the light sources was controlled to be identical. There is no obvious photoresponse that can be observed in In_6Se_7:P in Figure S4a−d. The resulted resistivity in each measurement condition for In_6Se_7:P is listed in Table S7 and the value is plotted in Figure S4e for comparison. The reduction in dark resistivity means the increase of electron concentration obtained by P doping. Figure S4f shows the experimental arrangement for the photo V−I measurement of the In_6Se_7:P series samples. In a highly conductive semiconductor, both conductivity and carrier concentration are high so that the incident photons cannot make a significant difference in excess carries (e.g., Δn) for enhancement of photoconductivity ($\Delta\sigma = \Delta n \cdot q \cdot \mu$, where q is the charge and μ is the mobility). The occurrence of n-type conductivity by P doping may be correlated with the formation of the P−Se bonding inside the In_6Se_7:P series compounds. In this bond style, the phosphorus dopant may act as a donor for providing electrons in the compound.

Furthermore, temperature-dependent resistivity results of the In_6Se_7:P series compounds from 20 to 300 K are shown in Figure 3c with semilogarithm and reciprocal-temperature scale. As the temperature increases, the resistivity decreases, showing the general semiconductor trend for all the In_6Se_7:P (P = 0%, 0.5%, 1%, and 5%) samples. This behavior is distinct from the other degenerate semiconductors or metals in that they show increased resistivity as the temperature is increased. The high carrier concentration to cause a degenerate semiconductor behavior can be observed in previous ternary compounds of $SnS_{1-x}Se_x$,[58] where a high amount of tin vacancies had rendered a large amount of hole density and made a degenerate p-type semiconductor of SnS and SnSe. In the case of the degenerate semiconductor, the resistivity is mostly influenced by the scattering events occurring between the high-density hot carriers. Consequently, an increase in the temperature results in an increase in resistivity. From Figure 3c, the Arrhenius equation, $\rho = \rho_0 \times \exp(\Delta E/K_B T)$, allows to estimate carrier activation energy (ΔE) and resistivity of

https://doi.org/10.1021/jacsau.3c00653
JACS Au 2024, 4, 58−71

$\frac{1000}{T} = 0$ (ρ_0) using a linear fit, where K_B is the Boltzmann constant. Carrier activation energy, ΔE, is the minimum energy required for an electron to thermally ionize from a donor level to E_C. According to the linear fits in Figure 3c, the activation energies for In_6Se_7:P (P = 0%, 0.5%, 1%, and 5%) are ΔE = 101 meV for P 0%, ΔE = 46 meV for P 0.5%, ΔE = 20 meV for P 1%, and ΔE = 13 meV for P 5%. The higher P doping causes the lower activation energy and the higher conductivity for rendering a larger electron concentration introduced in the layered In_6Se_7.

Since P doping has less effect on the structure and lattice alteration of In_6Se_7 observed from XRD and Raman, it can be inferred that impurities could have a greater influence on the materials. X-ray photoelectron spectroscopy (XPS) measurements were conducted to observed the bonding configuration of In_6Se_7:P. Concerning the Se 3d orbital in Figure 3d, the XPS peaks corresponding to the Se $3d_{3/2}$ (Se $3d_{5/2}$) for the In_6Se_7:P series are positioned at 54.9 eV (54.0 eV) for In_6Se_7 (P 0%) and decreases marginally to 54.5 eV (53.7 eV) as the P doping is increased to 5%. The increased scattering effect on the P-doped In_6Se_7 lattice results in the red shift and broadening of the Se $3d_{3/2}$ and Se $3d_{5/2}$ peaks as the P doping increases. In Figure S5a, the XPS of In 3d orbital is depicted, revealing that the positions of the $3d_{3/2}$ and $3d_{5/2}$ peaks (452.4 and 444.8 eV, respectively) do not demonstrate significant change but only a little red shift caused by P doping. The valence band (VB) in XPS spectra typically refers to the outermost energy levels for the filled electrons in In_6Se_7:P. The VB shifts from 0.54 eV (P 0%) to 0.13 eV (P 5%) in Figure S5b, confirming the *n*-type behavior and the raise of Fermi level to E_C, which is consistent with the results of Hall measurement and the measured activation energy ΔE. XPS spectra of electronic states from P were measured to provide experimental evidence, given that the valence states of P could potentially affect the carrier type in In_6Se_7. Regarding the P 2p orbital depicted in Figure 3e, the P doping obviously renders the appearance of a P 2p peak at ~133 eV and the intensity increases proportionally with the increase in the P doping amount. Due to the formation of P−Se bond (i.e., P = 0.5%, 1%, 5%), the energy position of the P 2p peak may upshift from a pure phosphorus position at ~130 eV to that of the P−Se bond at ~133 eV shown in Figure 3e. This result also indicates that the P atoms are bonded with the Se atoms (i.e., it will make *n* type doping) and not forming any In−P bond, similar to previous P−Se films or P_2Se_6-type materials.[59] In contrast, when bonding with In, the typical position of P 2p will shift to a lower energy of approximately 129 eV.[60,61] The formation of the P−Se bond results in the incorporation of extra electrons, hence elevating the abundance of electron carriers. Thus, larger P doping (In_6Se_7:P 0%, 0.5%, 1%, and 5%) could increase electron carrier concentration.

Kelvin probe measurements were conducted to evaluate surface potentials of the In_6Se_7:P series semiconductors. The measurement configuration of the Kelvin probe is illustrated in Figure 4a. The Kelvin probe technique is effective for determining surface-potential differences between materials.[62] The measurement also involves the estimate of work-function difference between various materials.[63,64] It is frequently used to evaluate the experimental Fermi level of semiconductor materials. The fundamental principle of contact potential difference (CPD) measurement using the Kelvin probe can be stated as follows: in the initial configuration, the tip and sample have their respective work functions (Φ_t and Φ_s) and Fermi levels (E_{ft} and E_F) in the left part of Figure 4a. The vacuum levels (E_{vac}) for both materials are in alignment. When the tip and sample are electrically connected (i.e., switch closed), the potential difference between the two materials will result in "current flow" until equilibrium is reached and then the Fermi levels of both the tip and sample become aligned. Thus, a contact potential difference (CPD) dominates between the tip and the sample, effectively shifting the vacuum energy levels E_{vac} of the combined tip−sample system. For this situation, the potential relationship between the tip and sample can be expressed as $\Phi_s = \Phi_t$ + CPD, where Φ represents the work function and CPD denotes the contact potential difference. As the sample and probe come into external connection, the two voltages become equal and generate a current flow (as the indicated direction in the middle part of Figure 4a) caused by an electrostatic force F between the sample and the probe. Essentially the electrostatic force F is responsible for the contact potential voltage V_{CPD} in semiconductors (eV_{CPD} in the case of eV) to identify the work function difference between the tip and sample. In the Kelvin probe's feedback loop, the electrostatic force F is compensated by applying $V_{DC} = V_{CPD}$ to lead to potential balance (see the right part of Figure 4a). From the value of V_{CPD} and known probe (tip) work function Φ_t, the work function of sample Φ_s is thus determined. Here, a mapping-enabled Kelvin probe system was used to investigate the Fermi level of the In_6Se_7:P compound and also evaluate the surface-potential homogeneity of the material. Figure 4b shows the experimental work function Φ_s (with representative error bars) for the multilayer samples of In_6Se_7:P (P = 0%, 0.5%, 1%, and 5%). The results are obtained using a thin sample with a thickness of around 40 nm. The inset image of Figure 4b displays the AFM result of a representative multilayer sample of In_6Se_7 with a thickness of ~37 nm. As shown in Figure 4b, the value of the work function decreases with the increase of the P content in the In_6Se_7:P series. The measured Kelvin probe work functions are Φ_s = 4695 meV for In_6Se_7, Φ_s = 4632 meV for In_6Se_7:P 0.5%, Φ_s = 4599 meV for In_6Se_7:P 1%, and Φ_s = 4566 meV for In_6Se_7:P 5%. The decrease of Φ_s means the increase of Fermi level and the increase of electron density, similar to the result of Hall-effect measurement.

In order to verify the surface-potential uniformity of the as-grown In_6Se_7:P series crystals, mapping-enabled Kelvin probe measurements are carried out for bulk In_6Se_7:P (P = 0%, 0.5%, 1%, and 5%) crystals over a 100 × 100 μm^2 scanning area at 300 K. Figure 4c depicts the work-function mapping and histogram of In_6Se_7. The In_6Se_7 material exhibits a central position at approximately 4695 meV, with a standard deviation spanning from 4702 to 4686 meV. This result indicates a highly uniform work function distribution, as illustrated in the inset. The Φ_s distribution and mapping of In_6Se_7:P 5% are shown in Figure 4d, which exhibits a visually consistent pattern with In_6Se_7. The central location of the distribution is around 4566 meV, with a deviation ranging from 4576 to 4558 meV. Figures S6a and b in the Supporting Information display the work-function histogram and mapping of In_6Se_7:P 0.5% and In_6Se_7:P 1%. The central values of Φ_s are 4623 meV (P 0.5%) and 4599 meV (P 1%), respectively. They also show potential uniformity as In_6Se_7 and In_6Se_7:P 5% displayed in Figure 4c and d. The consistency of Φ_s in a thin layer and in bulk observed from Figure 4b−d and from Figure S6a and b verifies the high quality of the as-grown In_6Se_7:P series crystals grown

https://doi.org/10.1021/jacsau.3c00653
JACS Au 2024, 4, 58−71

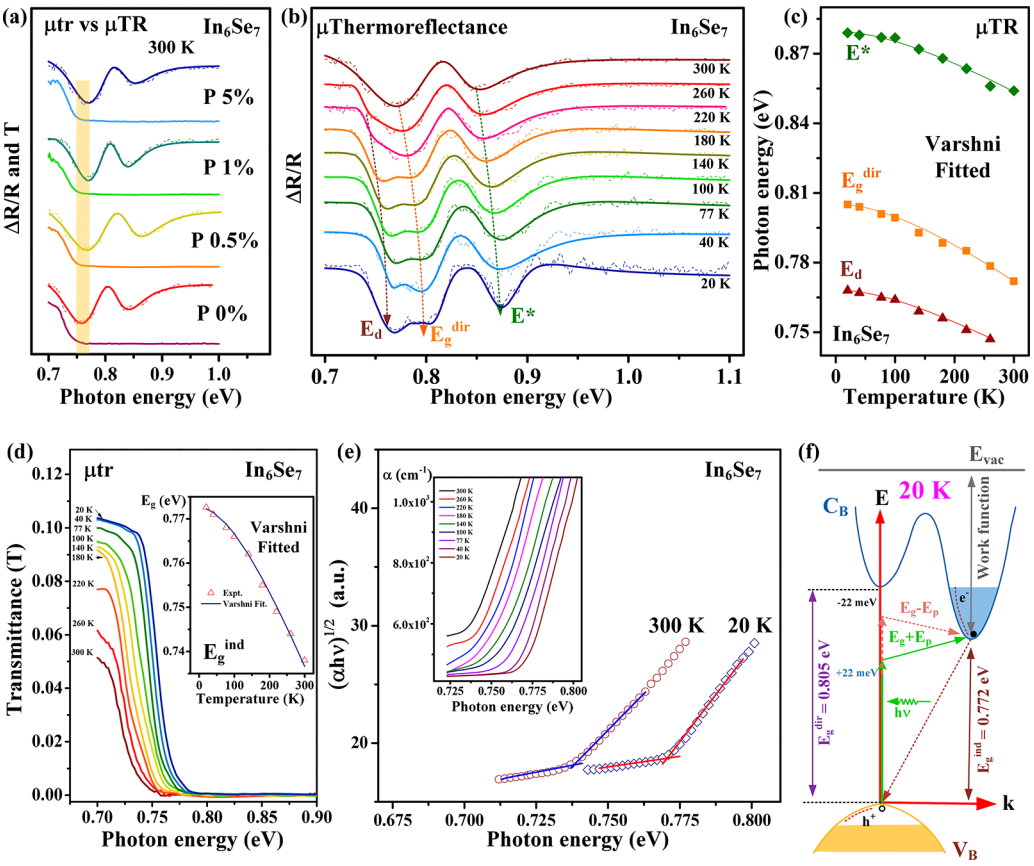

Figure 5. (a) Comparison of microtransmittance and microthermoreflectance spectra for the In_6Se_7:P series compounds at 300 K. (b) Temperature-dependent microthermoreflectance (μTR) spectra for In_6Se_7. (c) Temperature-dependent transition energies of E*, E_g^{dir} and E_d features detected by μTR from 20 to 300 K. The solid lines are those of the Varshni fits for the temperature-energy dependence. (d) Temperature-dependent microtransmittance (μtr) spectra of multilayer In_6Se_7 between 20 and 300 K. The inset shows the analysis of temperature-energy shift of indirect band gap of In_6Se_7. (e) Representative $[(\alpha h\nu)^{1/2}$ vs $h\nu]$ spectral analysis for multilayer In_6Se_7 involved the process of phonon emission and phonon absorption at selected temperatures of 300 and 20 K. The inset shows the temperature-dependent absorption curves (α) that derived from the μtr spectra in (d). (f) Experimental band-structure scheme of In_6Se_7 at 20 K.

by chemical vapor transport. They are suitable for making semiconductor (junction) devices for future applications.

To evaluate the optical band edge of the multilayer In_6Se_7:P series, microthermoreflectance (μTR) and microtransmittance (μtr) measurements were conducted and implemented from 20 to 300 K. Thermoreflectance (TR) measurement is a widely utilized technique in modulation spectroscopy that involves the analysis of critical-point transitions occurring in semiconductors.[65] Moreover, transmittance measurement is highly valuable for assessing optical absorption in the vicinity of band-edge energy portion.[66] The room-temperature μTR and μtr spectra of the In_6Se_7:P (P = 0%, 0.5%, 1%, and 5%) series between 0.7 and 1.0 eV are depicted in Figure 5a. The μTR and μtr spectra for each composition of In_6Se_7:P showed a similar shape and comparable energy. It indicates that the incorporation of the P dopant may not alter the band-edge structure of In_6Se_7. Essentially TR measurement characterizes semiconductors with a direct transition feature while transmittance measures materials with optical band-edge absorption and it is regardless of whether it is direct or indirect optical absorption from the band edge. As shown in Figure 5a, the energy of the direct band-edge transition by μTR (marked with yellow color) is larger than that of the absorption edge of transmittance (μtr) for each In_6Se_7:P compound. In_6Se_7 thus was inferred to be an indirect semiconductor with an indirect gap of ~0.732 eV measured by μtr and which is lower than the direct gap of ~0.772 eV obtained by μTR at 300 K. Figure 5b shows the temperature-dependent μTR spectra of multilayer In_6Se_7 with previous experimental setup[67] measured from 20 to 300 K. The short-dashed lines are the experimental spectra and solid curves are the least-squares fits of the TR data to a derivative Lorentzian line-shape function appropriate for the interband transitions of In_6Se_7.[66,67] At 20 K, at least three transition features denoted as E_d, E_g^{dir}, and E* can be detected in the μTR spectrum in Figure 5b. The transition features of E_d, E_g^{dir}, and E* revealed an energy reduction and approximately line-shape broadened behavior as the temperature increases from 20 up to 300 K. At 300 K, the E_d feature is ionized (disappearing), and only two transitions of E_g^{dir} and E* are detected by μTR. The transition energies of the E_d, E_g^{dir}, and E* features obtained by Lorentzian line-shape fits from 20 to 300 K are depicted in Figure 5c for comparison. The E_d feature is broadened and ionized at 260−300 K in Figure 5b. It may correlate with a valence band (V_B) to defect-state transition (e.g., Se vacancy for causing a donor state below E_C) in In_6Se_7. The E_g^{dir} feature in Figure 5b is assigned as a direct band-edge transition related to the direct gap of In_6Se_7 and E* and may correspond to a higher-energy critical point transition. The energies are E_d = 0.766 eV, E_g^{dir} = 0.805 eV, and E^* = 0.878 eV obtained from the spectral analysis of μTR

https://doi.org/10.1021/jacsau.3c00653
JACS Au 2024, 4, 58−71

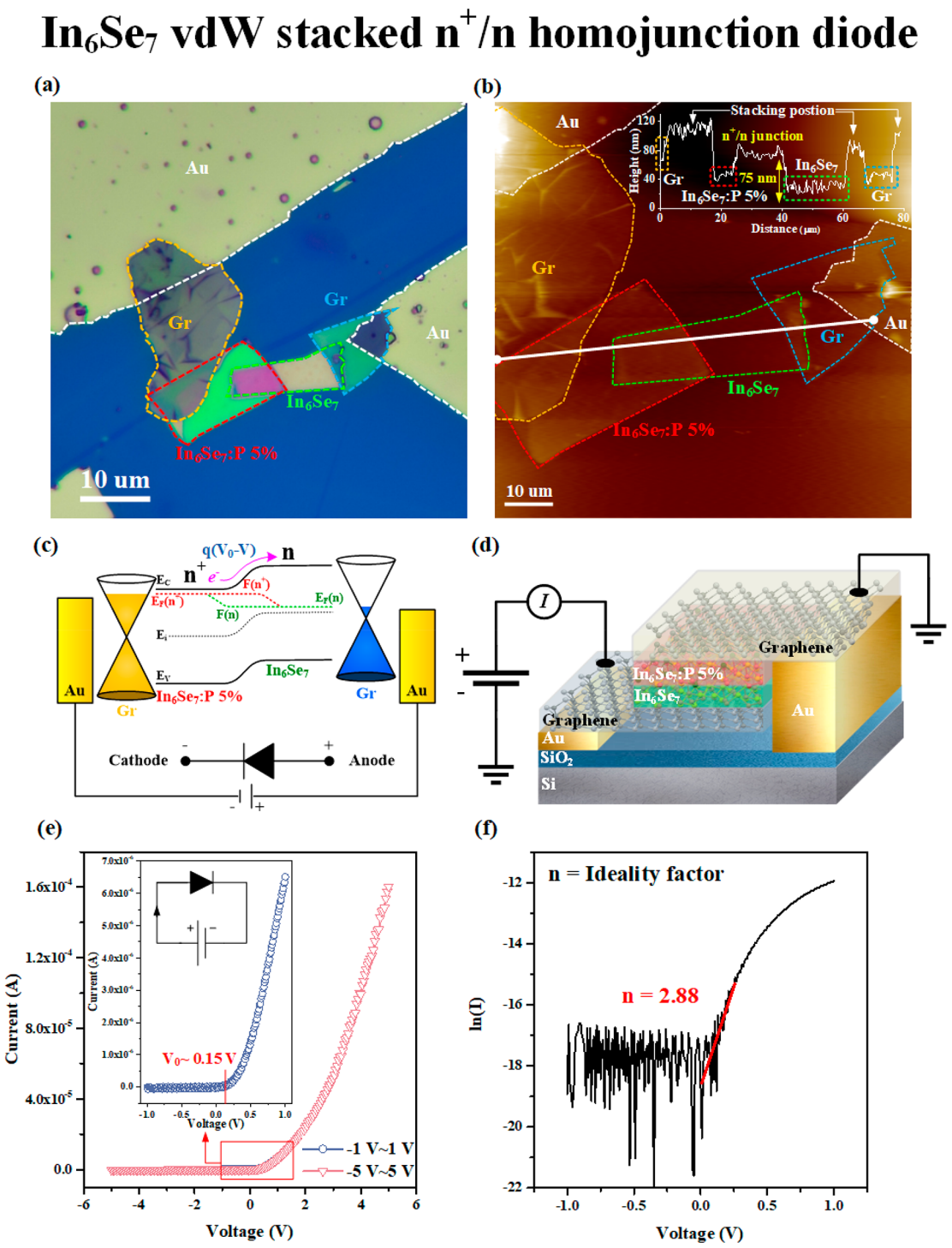

Figure 6. Fabrication and study of an In_6Se_7 vdW stacked n^+/n homojunction diode. (a) Microscope image of one (top) Au-graphehe-In_6Se_7:P 5%-In_6Se_7-graphene-Au (bottom) vdW stacked device. (b) AFM image and thickness profile for the In_6Se_7 vdW stacked n^+/n homojunction diode. (c) Energy band scheme of the In_6Se_7 vdW stacked junction under forward bias operation. (d) Electric connection and stacked structure of the In_6Se_7 n^+/n homojunction diode. (e) The V–I characteristic for the rectified junction under the voltage range of −5 to +5 V. The inset shows the small scanned range of −1 to +1 V to observe the cut-in voltage V_0 of the V–I curve. (f) The semilogarithm plot of the V–I curve to analyze ideality factor n of the In_6Se_7 vdW stacked diode.

spectrum at 20 K. The temperature-dependent transition energies of E_d, E_g^{dir}, and E* in Figure 5c can be analyzed using a Varshni empirical relationship as $E_g(T) = E_g(0) - \alpha \cdot T^2/(\beta + T)$,[68] where $E_g(0)$ denotes the transition energy at 0 K, α considers the strength of exciton−phonon interaction, and β is associated with the Debye temperature of the chalcogenide material. The Varshni fitted results are depicted as the solid lines in Figure 5c and the obtained values of fitting parameters are listed in Table S9. In the three transitions of E_d, E_g^{dir}, and E* of In_6Se_7, the Debye temperature β is comparable to be 275 ± 25 K while the strength of exciton−phonon interaction α of E_d is lower than the other features of E_g^{dir} and E* with a band-

https://doi.org/10.1021/jacsau.3c00653
JACS Au 2024, 4, 58−71

to-band transition. This behavior verifies that E_d is a defect transition (not for band to band) from the V_B maximum to a defect donor state below E_C.

Regarding to the indirect gap of In_6Se_7, Figure 5d reveals the transmittance absorption edge of μtr spectra lies between ~0.725 and ~0.775 eV from 300 K down to 20 K. The optical absorption coefficient α can be obtained from the transmittance (T) value using approximately a formula from the incident (I_0) and transmission (I_t) light intensity as $I_t = I_0 \cdot e^{-\alpha \cdot d}$, where the layer thickness used in this μtr experiment is about $d \sim 180$ nm (1.8×10^{-5} cm). The obtained absorption (α) spectra derived from Figure 5d are displayed in the inset of Figure 5e. They showed an absorption range lying between 0.725 eV (300 K) and 0.775 eV (20 K), and each absorption curve was analyzed to match a parabolic type of α proportional to $(h\nu\text{-}E_g)^n$ where n = 2 ± 0.1, i.e. indirect allow transition.[69] For an indirect absorption process, phonon emission or phonon absorption may be involved to assist the electronic transition from the V_B (or VB) maximum to conduction-band (C_B or E_C) minimum when the incident photon is absorbed. For a single phonon process, the absorption coefficient α is expressed as[69]

$$\alpha h\nu = \frac{A(h\nu - E_g + E_p)^2}{\exp(E_p/kT) - 1} + \frac{B(h\nu - E_g - E_p)^2}{1 - \exp(E_p/kT)} \quad (1)$$

where $h\nu$ is the energy of the incident photon, E_g is the indirect band gap, E_p is the energy of phonon assisting the transition, and A and B are constants. The first term and second terms of eq 1, respectively, indicate phonon-emission assisted ($E_g - E_p$) and phonon-absorption assisted ($E_g + E_p$) indirect-gap absorption. To evaluate the values of E_g and E_p from eq 1, the background absorption of α [see the inset of Figure 5e] is subtracted out. A square-root relation of $((\alpha h\nu)^{1/2}$ vs $h\nu)$ analysis could result in a lower-slope line obtained for $E_g - E_p$ and a higher slope line obtained for $E_g + E_p$ from their intersect energies as shown in Figure 5e using the T = 300 K and T = 20 K spectra as the representative data. The analyzed values of indirect gap E_g of multilayer In_6Se_7 from 20 to 300 K are depicted in the inset of Figure 5d, and the Varshni fitted parameters are also listed in Table S9 in the Supporting Information for comparison. The phonon energy E_p for assisting the indirect absorption is $E_p \approx 22$ meV from the linear analysis of $((\alpha h\nu)^{1/2}$ vs $h\nu)$ plot at each temperature. From the μtr and μTR measurements, the indirect and direct band gaps of multilayer In_6Se_7 are $E_g^{dir} = 0.805$ eV and $E_g = 0.772$ eV at 20 K and $E_g^{dir} = 0.772$ eV and $E_g = 0.732$ eV at 300 K, respectively. According to the measurement results of μTR, μtr, and Kelvin probe on the band structure related energies, an experimental band-edge scheme of In_6Se_7 is depicted in Figure 5f. At 20 K, the direct gap at the V_B maximum and a C_B valley of the same k (i.e., $E_g^{dir} = 0.805$ eV) is larger than the indirect band gap ($E_g = 0.772$ eV) with the CB minimum located at another k direction. The indirect band gap transition may occur with absorption $[h\nu = (E_g + E_p)]$ or emission $[h\nu = (E_g - E_p)]$ of a phonon with energy about $E_p = 22$ meV when the photon $h\nu$ is incident to In_6Se_7. The room-temperature work function (Φ_s, from E_F to E_{vac}) is about 4.7 eV measured by a Kelvin probe, and it will increase as the temperature is decreased. Figure S7 in the Supporting Information also displays the individual band scheme of each In_6Se_7:P (P = 0, 0.5, 1, and 5%) compound that was evaluated using μTR, μtr, activation energy, and work function measurements As the doped content of P increases, the band gap still remains unchanged (i.e., 0.732 eV at 300 K) but the work function and activation energy of In_6Se_7:P are decreased to enhance the electron carrier concentration with doping. As compared to In_6S_7 having a band gap of ~0.93 eV,[70] the indirect and direct band gaps of In_6Se_7 (i.e., 0.73~0.78 eV) may efficiently absorb more NIR photons for further solar energy and electronic device applications.

As the phosphorus doping obviously influences the Fermi level and carrier concentration of the n-type In_6Se_7, a rectified n^+/n homojunction was thus fabricated by stacking the van der Waals (vdW) In_6Se_7/In_6Se_7:P 5% multilayers for showing the fundamental diode behavior for further device applications. Figure 6a shows the microscope image of a prototype of an In_6Se_7 vdW stacked n^+/n homojunction diode. The vdW device structure is composed of multilayer graphene (graphite)-In_6Se_7:P 5% (n^+)-In_6Se_7 (n)-multilayer graphene (graphite) with a layer thickness of each material of around 30−40 nm. Masked and evaporated gold film on SiO_2/Si substrate was first prepared for the electrical metal electrodes. The function of graphene is to make better ohmic contact between In_6Se_7 and the Au electrode. The AFM result and thickness profile of the vdW stacked n^+/n homojunction structure is shown in Figure 6b. Essentially, the thickness of the stacked junction is ~75 nm, corresponding to an In_6Se_7:P 5% (40 nm) layer covered on an In_6Se_7 (35 nm) nanosheet. Figure 6c and d, respectively, shows the band diagram under forward-bias operation and the 3D scheme of vdW stacked n/n^+ homojunction diode of In_6Se_7. When a forward bias is supplied to the vdW device, the voltage of the n-In_6Se_7 side is higher than that of n^+-In_6Se_7 and the electrons of conduction in n^+-In_6Se_7 will overcome a potential barrier V_0 to flow into the n-In_6Se_7 region for making forward current. The situation is dominated by diode equation $I = I_0 \cdot \exp[q(V - V_0)/(n \cdot k \cdot T)]$, where I_0 is the reversed saturation current, V_0 the built-in potential (V_{bi}), and n is the ideality factor for the n^+/n homojunction diode. At the forward-bias condition of the n^+/n junction diode, the Fermi levels of $E_F(n)$ and $E_F(n^+)$ are not identical and they become quasi-Fermi levels of F(n) and F(n^+) located near the junction region (i.e., transition region) in Figure 6c. The space gradient of F(n) and F(n^+) could make forward current flow of the In_6Se_7 vdW diode under forward-bias operation. Figure 6e shows the V−I curves for the In_6Se_7 stacked n^+/n homojunction diode with two scanned ranges of −5 to +5 V (red-triangle line) and −1 to +1 V (blue-circle line). The result shows a clear rectified behavior of the V−I data that detected in the diode and a cutoff region can extend over the reversed-bias region of −5 V. The V−I curve of the −1 to +1 V (blue-circle line) range shown in the inset of Figure 6e identifies the cut-in voltage of $V_0 \approx 0.15$ V is matched well with the work function difference between In_6Se_7 and In_6Se_7:P 5% measured by Kelvin probe. The logarithm current plot vs applied voltage of the n^+/n junction diode by using the analysis of diode equation is depicted in Figure 6f. The linear slope of the start-up portion for the V−I curve gives an ideality factor of about n = 2.88 for the diode (i.e., n = 1 for an ideal diode). The reversed saturation current I_0 is obtained as about 15 nA in the reversed-bias region. The experimental data showed a well-behaved electrical performance for the prototype of the In_6Se_7 vdW stacked n^+/n homojunction diode. Further improvement of surface condition, defects, and doping impurities can be done to promote the electrical function of the multilayered In_6Se_7 vdW junction device.

https://doi.org/10.1021/jacsau.3c00653
JACS Au 2024, 4, 58−71

3. CONCLUSION

A novel vdW stacked multilayer In_6Se_7 n^+/n homojunction diode is successfully fabricated in this work. Before developing the homojunction device, high-quality phosphorus-doped In_6Se_7 crystals with different P compositions of P = 0%, 0.5%, 1%, and 5% were grown by the CVT method with ICl_3 as the transport agent. XRD and HRTEM measurements identified that the In_6Se_7:P series compounds are crystallized in the same monoclinic structure with comparable values of lattice constants. The μRaman results of multilayer In_6Se_7:P revealed similar vibration modes for the whole series and only showed a broadened peak feature as the P content is increased. Excepting undoped In_6Se_7, one additional peak at ~171 cm^{-1} which is associated with the P−Se bonding was detected for the P-doped In_6Se_7 (P = 0.5, 1, and 5%). The peak intensity of 171 cm^{-1} mode enhances as the increase of P doping to verify the doping effect and carrier type of the In_6Se_7:P. XPS results of valence band V_B and P 2p orbital identified the raise of Femi level and the increase of electron concentration (i.e., *n* type) as the P dopant content is increased. Hall-effect and temperature-dependent resistivity measurements confirmed *n*-type conductivity, the increase of electron density, and the decrease of electron activation energy as the P doping content is increased in the In_6Se_7:P (P = 0, 0.5, 1, and 5%) series. The increase of Fermi level (close to conduction band edge E_C) means the increase of electron concentration and the decrease of work function as the P content increases. The result was certified by surface potential and work function measurements performed by Kelvin probe. For the evaluation of experimental band edge, the results of μtr and μTR indicate that In_6Se_7 is an indirect semiconductor which possessing an indirect gap of E_g ~ 0.732 eV (0.772 eV) and a direct gap of ~0.772 eV (~0.805 eV) at 300 K (20 K). In comparison with its In_6S_7 and InSe counterparts (band gap 0.93 and 1.24 eV), In_6Se_7 can absorb more NIR photons available for photoelectric conversion under sunlight. A novel vdW stacked multilayer In_6Se_7 n^+/n homojunction diode was first made by stacking multilayer In_6Se_7:P 5% on pure In_6Se_7 with multilayered graphene as the contact medium with Au electrode. The *V*−*I* curve shows good performance of the rectified behavior of the In_6Se_7 diode with an ideality factor of n = 2.88 and the reversed leakage current down to I_0 = 15 nA. The fundamental homojunction can be as a device reference for future electronics or optoelectronics applications.

4. MATERIALS AND METHODS

Synthesis and Crystallization

The growth and characterization of In_6Se_7 crystals doped with varying concentrations of phosphorus (P = 0%, 0.5%, 1%, and 5%) were investigated in this study. The crystals were grown using high-purity elements: 99.99% pure In (6 mm shot), 99.999% pure Se (1−3 mm shot), and 99.9999% pure P (1−5 mm shot). A mixture of 10 g of elements and 1−2 g of ICl_3 was introduced into a quartz tube (outer diameter 22 mm, inner diameter 17 mm, and length 20 cm), which was then evacuated to 10^{-6} Torr (after cooling with liquid nitrogen) and sealed. The mixture was placed in a three-zone horizontal tube furnace, heated to 700 °C, held for 3 days for compound synthesized, and then set to a growth temperature of 600 °C with a gradient of −5 °C/cm^{-1} for 14 days to produce single-crystal samples. The In_6Se_7:P series compound can be subjected to mechanical exfoliation using Scotch tape due to the weakened van der Waals forces, enabling its transfer onto a SiO_2/Si substrate (8 × 8 × 0.3 mm^3) for further electrical and optical measurements. Both the as-grown crystals and exfoliated samples were protected from oxidation by being stored in a vacuum-sealed chamber. The thickness of each exfoliated sample was gauged by using atomic force microscopy (AFM).

Material Structure Characterization

Structural analysis was performed by X-ray diffraction (XRD) using a Bruker D2 PHASER XE-T XRD instrument equipped with a Cu Kα line (λ = 0.15406 nm) X-ray source. The crystals were precisely ground to perform X-ray diffraction (XRD) measurements. The measurement range was from 10° to 60° with a step size of 0.02°. For TEM/EDS mapping, 1 g of the sample was ultrasonically dispersed to the nanoscale, deposited onto a copper grid, and then measured using a FEI Tecnai G2 F-20 S-TWIN TEM/EDS system. The EDS spectra and mapping were measured through STEM mode with the α = 15°. The X-ray photoelectron spectroscopy (XPS) analysis was conducted using a ULVAC-PHI. Inc. spectrometer to quantify material element's composition and energy state. Micro-Raman measurements were performed using a ProTrusTech Ramaker micro-Raman scattering spectrometer equipped with a 532 nm solid-state laser, an Olympus objective (50 ×), and an Andor CCD spectrometer (1200 grooves/mm). Atomic force microscopy (AFM) measurements of the multilayers are carried out using a NanoMagnetics ezAFM instrument with a noncontact measurement mode over a 10 × 10 μm area.

Electrical Characterization

Hot probe and photovoltage−current (photo *V*−*I*) measurements were carried out in a two-point measurement configuration. The Seebeck coefficient of the material was calculated using hot probe measurements, while photovoltage−current responses were studied under three conditions: (1) in the dark, (2) under light-emitting diode (LED) illumination, and (3) under tungsten halogen lamp (THL) illumination. The measurements of the photo *V*−*I* were conducted using a Keithley 230 voltage source and a Keithley 6485 current meter. The Hall-effect and resistivity measurements were performed using a van der Pauw method and a Keithley 6220 current source with a Keithley 2182 voltage meter at a magnetic field of 0.7 T to perform Hall voltage detection. The resistivity measurements under varying temperature conditions were performed using stainless steel substrates with adhesive tape attached (i.e., for insulating) to connect four electrodes and a Lakeshore 335 temperature controller and CTI cryogenic compressor acted as the temperature control from 20 to 300 K. Kelvin probe measurements were performed using the SKP5050 instrument developed by KP Technology. A probe tip size of 1−50 μm can be chosen for measurement, and calibration with a gold-coated substrate (work function ϕ_{Au} ~ 5.1 eV) was performed to correct environmental factors. The probe's work function is Be (ϕ_{tip} ~ 4.9 eV) and can be compared with the gold work function ϕ_{Au} of the substrate to obtain the semiconductor work function ϕ_s from the contact potential difference (CPD) between probe tip and the semiconductor.

Optical Characterization

Microthermoreflectance (μTR) measurement with a 150 W tungsten halogen lamp was utilized for modulation spectroscopy measurement. A 0.2 m Photon Technology International

https://doi.org/10.1021/jacsau.3c00653
JACS Au 2024, 4, 58−71

monochromator with 600 grooves mm^{-1} grating was used to disperse the incident white light, and the light-guiding microscope (LGM) directs the monochromatic light to the sample. The In_6Se_7:P series multilayers were exfoliated on a quartz substrate with evaporated gold film, and the reflected light from the sample surface was passed through the LGM and then conducted using a quartz fiber to an InGaAs photodetector. A 4 Hz on/off heating current (approximately 0.4 A) was periodically supplied to the Au heater for modulation of the lattice constant and band gap thermally. Detection of a small signal by using an NF 5610B lock-in amplifier was employed. Using a quartz window chamber, a Lakeshore 335 temperature controller, and a CTI cycle liquid helium cryogenic compressor, temperature-dependent micro-thermoreflectance (μTR) measurement from 20 to 300 K can be performed. In the microtransmittance (μtr) measurement apparatus, the same monochromator and LGM setup as μTR experiment was used. The multilayer sample was exfoliated to cover a light-transmitting hole of the copper holder. The transmission light from the sample was focused to a quartz optical fiber which connected to an InGaAs photodetector. Phase-sensitive detection was achieved using an NF 5610B lock-in amplifier. A Janis open-circled liquid-helium cryostat equipped with a Lakeshore 335 thermometer controller was used to facilitate temperature-dependent measurements from low temperatures to room temperature.

■ ASSOCIATED CONTENT

Supporting Information

The Supporting Information is available free of charge at https://pubs.acs.org/doi/10.1021/jacsau.3c00653.

Experimental section, results of energy dispersive X-ray spectroscopy, XRD, HRTEM, temperature-dependent Raman spectroscopy, Seebeck coefficient, photo $V-I$ curves, XPS spectra, work function mapping, temperature-dependent direct and indirect gaps, and band-structure diagram of each In_6Se_7:P (P = 0, 0.5, 1 and 5%) compound (PDF)

■ AUTHOR INFORMATION

Corresponding Author

Ching-Hwa Ho − *Graduate Institute of Applied Science and Technology, National Taiwan University of Science and Technology, Taipei 106, Taiwan; Taiwan Consortium of Emergent Crystalline Materials, National Science and Technology Council, Taipei 106, Taiwan;* orcid.org/0000-0002-7195-208X; Phone: +886-2-27303772; Email: chho@mail.ntust.edu.tw; Fax: +886-2-27303733

Authors

Yu-Hung Peng − *Graduate Institute of Applied Science and Technology, National Taiwan University of Science and Technology, Taipei 106, Taiwan*

Luthviyah Choirotul Muhimmah − *Graduate Institute of Applied Science and Technology, National Taiwan University of Science and Technology, Taipei 106, Taiwan*

Complete contact information is available at: https://pubs.acs.org/10.1021/jacsau.3c00653

Author Contributions

C.-H.H. conceives the idea and supervises the optical and structural characterization. C.-H.H. and Y.-H.P. grew the crystals. Y.-H. P. is responsible for the methodology in HRTEM, XRD, Raman, and Kelvin probe experiments. L. C. M. is responsible for the methodology in transmittance and thermoreflectance measurements. C.-H.H., L.C.M, and Y.-H.P. wrote the manuscript. C.-H.H. is also responsible for funding acquisition, work supervision, writing review, and editing. CRediT: **Yu-Hung Peng** data curation, formal analysis, investigation, methodology; **Luthviyah Choirotul Muhimmah** data curation, investigation, methodology, writing-original draft; **Ching-Hwa Ho** conceptualization, funding acquisition, project administration, resources, supervision, writing-original draft, writing-review & editing.

Notes

The authors declare no competing financial interest.

■ ACKNOWLEDGMENTS

The authors would like to acknowledge the funding support of the National Science and Technology Council, Taiwan, under the grant numbers NSTC 112-2124-M-011-001, NSTC 110-2221-E-011-101-MY3, NSTC 111-2622-E-011-021, NSTC 112-2622-E-011-025, and NSTC 112-2923-E-011-002-MY3.

■ REFERENCES

(1) Cai, H.; Gu, Y.; Lin, Y.-C.; Yu, Y.; Geohegan, D. B.; Xiao, K. Synthesis and Emerging Properties of 2D Layered III−VI Metal Chalcogenides. *Appl. Phys. Rev.* **2019**, *6*, No. 041312.

(2) Ho, C.-H.; Hsieh, M.-H.; Wu, C.-C. Photoconductance and Photoresponse of Layer Compound Photodetectors in The UV-Visible Region. *Rev. Sci. Instrum.* **2006**, *77*, 113102.

(3) Yang, H.-W.; Hsieh, H.-F.; Chen, R.-S.; Ho, C.-H.; Lee, K.-Y.; Chao, L.-C. Ultraefficient Ultraviolet and Visible Light Sensing and Ohmic Contacts in High-Mobility InSe Nanoflake Photodetectors Fabricated by The Focused Ion Beam Technique. *ACS Appl. Mater. Interfaces* **2018**, *10*, 5740−5749.

(4) Chuang, C.-A.; Lin, M.-H.; Yeh, B.-X.; Ho, C.-H. Curvature-Dependent Flexible Light Emission from Layered Gallium Selenide Crystals. *RSC Adv.* **2018**, *8*, 2733−2739.

(5) Ho, C.-H.; Lin, S.-L. Optical Properties of The Interband Transitions of Layered Gallium Sulfide. *J. Appl. Phys.* **2006**, *100*, No. 083508.

(6) Muhimmah, L. C.; Peng, Y.-H.; Yu, F.-H.; Ho, C.-H. Near-Infrared to Red-Light Emission and Carrier Dynamics in Full Series Multilayer $GaTe_{1-x}Se_x$ ($0 \le x \le 1$) with Structural Evolution. *npj 2D Mater. Appl.* **2023**, *7*, 3.

(7) Lu, Y.-Y.; Guo, C.-R.; Yeh, H.-L.; Chen, H.-W.; Kuo, C.-C.; Hsu, J.-H.; Jhou, J.; Huang, Y.-T.; Hsieh, S.-H.; Chen, C.-H.; Ho, C.-H.; Sankar, R.; Chou, F.-C. Multilayer GaSe/InSe Heterointerface-Based Devices for Charge Transport and Optoelectronics. *ACS Appl. Nano Mater.* **2020**, *3*, 11769−11776.

(8) Ho, C.-H.; Chiou, M.-C.; Herninda, T. M. Nanowire Grid Polarization and Polarized Excitonic Emission Observed in Multilayer GaTe. *J. Phys. Chem. Lett.* **2020**, *11*, 608−617.

(9) Ho, C.-H. Thickness-dependent Carrier Transport and Optically Enhanced Transconductance Gain in III-VI Multilayer InSe. *2D Mater.* **2016**, *3*, No. 025019.

(10) Afzaal, M.; O'Brien, P. Recent Developments in II−VI and III−VI Semiconductors and Their Applications in Solar Cell. *J. Mater. Chem.* **2006**, *16*, 1597−1602.

(11) Ho, C.-H.; Chu, Y.-J. Bending Photoluminescence and Surface Photovoltaic Effect on Multilayer InSe 2D Microplate Crystals. *Adv. Opt. Mater.* **2015**, *3*, 1750−1758.

(12) Pan, Y.; Zhao, Q.; Gao, F.; Dai, M.; Gao, W.; Zheng, T.; Su, S.; Li, J.; Chen, H. Strong In-Plane Optical and Electrical Anisotropies of Multilayered γ-InSe for High-Responsivity Polarization-Sensitive Photodetectors. *ACS Appl. Mater. Interfaces* **2022**, *14*, 21383−21391.
(13) Ali, Z.; Mirza, M.; Cao, C.; Butt, F. K.; Tanveer, M.; Tahir, M.; Aslam, I.; Idrees, F.; Safdar, M. Wide Range Photodetector Based on Catalyst Free Grown Indium Selenide Microwires. *ACS Appl. Mater. Interfaces* **2014**, *6*, 9550−9556.
(14) Lu, Y.; Warner, J. H. Synthesis and Applications of Wide Bandgap 2D Layered Semiconductors Reaching the Green and Blue Wavelengths. *ACS Appl. Electron. Mater.* **2020**, *2*, 1777−1814.
(15) Chuang, C.-A.; Yu, F.-H.; Yeh, B.-X.; Ummah, A. M.; Rosyadi, A. S.; Ho, C.-H. Visible White-Light Emission and Carrier Dynamics Observed in Full-Series $GaSe_{1-x}S_x$ ($0 \leq x \leq 1$) Multilayers. *Adv. Optical Mater.* **2023**, 2301032.
(16) Ho, C.-H.; Chan, C.-H.; Tien, L.-C.; Huang, Y.-S. Direct Optical Observation of Band-Edge Excitons, Band Gap, and Fermi Level in Degenerate Semiconducting Oxide Nanowires In_2O_3. *J. Phys. Chem. C* **2011**, *115*, 25088−25096.
(17) Murali, A.; Barve, A.; Leppert, V. J.; Risbud, S. H.; Kennedy, I. M.; Lee, H. W. H. Synthesis and Characterization of Indium Oxide Nanoparticles. *Nano Lett.* **2001**, *1*, 287−289.
(18) Ho, C.-H. Enhanced Photoelectric-Conversion Yield in Niobium-Incorporated In_2S_3 with Intermediate Band. *J. Mater. Chem.* **2011**, *21*, 10518−10524.
(19) Ho, C.-H. Growth and Characterization of Near-Band-Edge Transitions in β-In_2S_3 Single Crystals. *J. Cryst. Growth* **2010**, *312*, 2718−2723.
(20) Ho, C.-H.; Lin, M.-H.; Wang, Y.-P.; Huang, Y.-S. Synthesis of In_2S_3 and Ga_2S_3 Crystals for Oxygen Sensing and UV Photodetection. *Sens. Actuator A Phys.* **2016**, *245*, 119−126.
(21) Ho, C.-H.; Wang, Y.-P.; Chan, C.-H.; Huang, Y.-S.; Li, C.-H. Temperature-dependent Photoconductivity in Single Crystals. *J. Appl. Phys.* **2010**, *108*, No. 043518.
(22) Ho, C.-H.; Chen, Y.-C.; Pan, C.-C. Structural Phase Transition and Erasable Optically Memorized Effect in Layered γ-In_2Se_3 Crystals. *J. Appl. Phys.* **2014**, *115*, No. 033501.
(23) Ho, C.-H.; Chen, Y.-C. Thickness-Tunable Band Gap Modulation in γ-In_2Se_3. *RSC Adv.* **2013**, *3*, 24896−24899.
(24) Ho, C.-H. Amorphous Effect on The Advancing of Wide-Range Absorption and Structural-Phase Transition in γ-In_2Se_3 Polycrystalline Layers. *Sci. Rep.* **2014**, *4*, 4764.
(25) Safdar, M.; Waqas, M.; Jabeen, N.; Saeed, A.; Butt, F. K.; Murtaza, S.; Mirza, M. Fabrication of In_2Te_3 Nanowalls Garnished with Zno Nanoparticles and Their Field Emission Behavior. *Mater. Chem. Phys.* **2022**, *290*, 126510.
(26) Yao, J.; Deng, Z.; Zheng, Z.; Yang, G. Stable, Fast UV−Vis−NIR Photodetector with Excellent Responsivity, Detectivity, and Sensitivity Based on α-In_2Te_3 Films with a Direct Bandgap. *ACS Appl. Mater. Interfaces* **2016**, *8*, 20872−20879.
(27) Segura, A.; Guesdon, J. P.; Besson, J. M.; Chevy, A. Photovoltaic Effect in InSe Application to Solar Energy Conversion. *Revue de Physique Appliquée* **1979**, *14*, 253−257.
(28) Feng, W.; Zheng, W.; Chen, X.; Liu, G.; Cao, W.; Hu, P. Solid-State Reaction Synthesis of a InSe/$CuInSe_2$ Lateral p−n Heterojunction and Application in High Performance Optoelectronic Devices. *Chem. Mater.* **2015**, *27*, 983−989.
(29) Shang, J.; Pan, L.; Wang, X.; Li, J.; Deng, H.-X.; Wei, Z. Tunable Electronic and Optical Properties of InSe/InTe van der Waals Heterostructures Toward Optoelectronic Applications. *J. Mater. Chem. C* **2018**, *6*, 7201−7206.
(30) Ando, K.; Katsui, A. Optical Properties and Photovoltaic Device Applications of Inse Films. *Thin Solid Films* **1981**, *76*, 141−148.
(31) Di Giulio, M.; Micocci, G.; Rella, R.; Siciliano, P.; Tepore, A. Optical Absorption and Photoconductivity in Amorphous Indium Selenide Thin Films. *Thin Solid Films* **1987**, *148*, 273−278.
(32) Yuan, H.; Zhang, Y.-W. Role of Ferroelectric In_2Se_3 in Polysulfide Shuttling and Charging/Discharging Kinetics in Lithium/Sodium−Sulfur Batteries. *ACS Appl. Mater. Interfaces* **2022**, *14*, 16178−16184.
(33) Balkanski, M.; Julien, C.; Jouanne, M. Electron and Phonon Aspects in A Lithium Intercalated InSe Cathode. *J. Power Sources* **1987**, *20*, 213−219.
(34) Karmakar, G.; Pathak, D. D.; Tyagi, A.; Mandal, B. P.; Wadawale, A. P.; Kedarnath, G. Molecular Precursor Mediated Selective Synthesis of Phase Pure Cubic InSe and Hexagonal In_2Se_3 Nanostructures: New Anode Materials for Li-Ion Batteries. *Dalton Trans.* **2023**, *52*, 6700−6711.
(35) Feng, W.; Wu, J.-B.; Li, X.; Zheng, W.; Zhou, X.; Xiao, K.; Cao, W.; Yang, B.; Idrobo, J.-C.; Basile, L.; Tian, W.; Tan, P. H.; Hu, P. A. Ultrahigh Photo-Responsivity and Detectivity in Multilayer InSe Nanosheets Phototransistors with Broadband Response. *J. Mater. Chem. C* **2015**, *3*, 7022−7028.
(36) Ben Nasr, T.; Ben Abdallah, H.; Bennaceur, R. First-principles Study of The Electronic and The Optical Properties of In_6Se_7 Compound. *Physica B Condens. Matter* **2010**, *405*, 3427−3432.
(37) Han, G.; Chen, Z.-G.; Drennan, J.; Zou, J. Indium Selenides: Structural Characteristics, Synthesis and Their Thermoelectric Performances. *Small* **2014**, *10*, 2747−2765.
(38) Ke, F.; Liu, C.; Gao, Y.; Zhang, J.; Tan, D.; Han, Y.; Ma, Y.; Shu, J.; Yang, W.; Chen, B.; Mao, H.-K.; Chen, X.-J.; Gao, C. Interlayer-glide-driven Isosymmetric Phase Transition in Compressed In_2Se_3. *Appl. Phys. Lett.* **2014**, *104*, 212102.
(39) Ornelas, R. E.; Avellaneda, D.; Shaji, S.; Castillo, G. A.; Roy, T. K. D.; Krishnan, B. In_6Se_7 Thin Films by Heating Thermally Evaporated Indium and Chemical Bath Deposited Selenium Multilayers. *Appl. Surf. Sci.* **2012**, *258*, 5753−5758.
(40) Li, J.; Li, H.; Niu, X.; Wang, Z. Low-Dimensional In_2Se_3 Compounds: From Material Preparations to Device Applications. *ACS Nano* **2021**, *15*, 18683−18707.
(41) El-Kabnay, N.; Shaaban, E. R.; Afify, N.; Abou-Sehly, A. Optical and Physical Properties of Different Composition of In_xSe_{1-x} Thin Films. *Physica B Condens. Matter* **2008**, *403*, 31−36.
(42) Abd El-Moiz, A. B.; Afify, N.; Hafiz, M. DTA Studies on The Crystallization of In_xSe_{1-x} Chalcogenide Glasses. *Physica B Condens. Matter* **1992**, *182*, 33−41.
(43) Imai, K.; Suzuki, K.; Haga, T.; Hasegawa, Y.; Abe, Y. Phase Diagram of In—Se System and Crystal Growth of Indium Monoselenide. *J. Cryst. Growth* **1981**, *54*, 501−506.
(44) Errandonea, D.; Martínez-García, D.; Segura, A.; Chevy, A.; Tobias, G.; Canadell, E.; Ordejon, P. High-Pressure, High-Temperature Phase Diagram of InSe: A Comprehensive Study of The Electronic and Structural Properties of The Monoclinic Phase of InSe Under High Pressure. *Phys. Rev. B* **2006**, *73*, 235202.
(45) Ferlat, G.; Martínez-García, D.; Miguel, A. S.; Aouizerat, A.; Muñoz-Sanjosé, V. High Pressure Research: An International Journal. *High Press Res.* **2004**, *24*, 111−116.
(46) Eddike, D.; Ramdani, A.; Brun, G.; Tedenac, J. C.; Liautard, B. Phase Diagram Equilibria In_2Se_3−Sb_2Se_3 Crystal Growth of The β-In_2Se_3 Phase ($In_{1.94}Sb_{0.06}Se_3$). *Mater. Res. Bull.* **1998**, *33*, 519−523.
(47) Melnychuk, T. A.; Strebegev, V. M.; Vorobets, G. I. Laser Synthesis of Thin Layers of In_4Se_3, In_4Te_3 and Modification of Their Structure and Characteristics. *Appl. Surf. Sci.* **2007**, *254*, 1002−1006.
(48) Anuroop, R.; Pradeep, B. Fabrication of n-In_6Se_7:Sn/P-$CuInSe_2$ Heterojunction Diode on FTO Coated Glass Substrates Using Reactive Evaporation Technique. *Solid State Commun.* **2020**, *306*, 113773.
(49) Hogg, J. H. C. The Crystal Structure of In_6Se_7. *Acta. Crystallogr. B. Struct. Sci. Cryst. Eng. Mater.* **1971**, *27*, 1630−1634.
(50) Walther, R.; Deiseroth, H. Redetermination of The Crystal Structure of Hexaindium Heptaselenide, In_6Se_7. *J. Z. fur Krist.-Cryst. Mater.* **1995**, *210*, 359−359.
(51) El-Deeb, A.; Metwally, H.; Shehata, H. Structural and Electrical Properties of In_6Se_7 Thin Films. *J. Phys. D* **2008**, *41*, 125305.
(52) Li, J.; Xia, B.; Wang, T.; Gao, D. Robust Ferromagnetism in Cr-Doped ReS_2 Nanosheets Demonstrated by Experiments and Density Functional Theory Calculations. *Nanotechnology* **2020**, *31*, 175702.

https://doi.org/10.1021/jacsau.3c00653
JACS Au 2024, 4, 58−71

(53) Rosyadi, A. S.; Chan, A. H.-Y.; Li, J.-X.; Liu, C.-H.; Ho, C.-H. Formation of van der Waals Stacked p−n Homojunction Optoelectronic Device of Multilayered $ReSe_2$ by Cr Doping. *Adv. Opt. Mater.* **2022**, *10*, 2200392.
(54) Muhimmah, L. C.; Ho, C.-H. Dual Phase Two-color Emission Observed in van der Waals GaTe Planes. *Appl. Surf. Sci.* **2021**, *542*, 148593.
(55) Zhu, C.; Yu, W.; Zhang, S.; Chen, J.; Liu, Q.; Li, Q.; Wang, S.; Hua, M.; Lin, X.; Yin, L.; et al. Hexaindium Heptasulfide/Nitrogen and Sulfur Co-Doped Carbon Hollow Microspindles with Ultrahigh-Rate Sodium Storage through Stable Conversion and Alloying Reactions. *Adv. Mater.* **2023**, *35*, 2211611.
(56) Weszka, J.; Daniel, Ph.; Burian, A. M.; Burian, A.; Żelechower, M. Temperature Dependence of Raman Scattering in Amorphous Films of $In_{1-x}Se_x$ alloys. *Solid State Commun.* **2001**, *119*, 533−537.
(57) Phillips, R. T.; Wolverson, D.; Burdis, M. S.; Fang, Y. Observation of Discrete Molecular Structures in Glassy P_xSe_{1-x} by Raman Spectroscopy. *Phys. Rev. Lett.* **1989**, *63*, 2574.
(58) Herninda, T. M.; Hsu, C. E.; Hsueh, H.-C.; Ho, C.-H. Structural, Opto-Electrical, and Band-Edge Properties of Full-Series Multilayer $SnS_{1-x}Se_x$ ($0 \leq x \leq 1$) Compounds with Strong In-Plane Anisotropy. *Mater. Today Adv.* **2023**, *18*, 100379.
(59) Huang, Y.-F.; Yang, Y.-C.; Tuan, H.-Y. Construction of Strongly Coupled Few-layer $FePSe_3$-CNT Hybrids for High Performance Potassium-Ion Storage Devices. *Chem. Eng. J.* **2023**, *451*, 139013.
(60) Moulder, J. F.; Stickle, W. F.; Sobol, P. E.; Bomben, K. D. *Handbook of X-ray Photoelectron Spectroscopy*; Physical Electronics Division, Perkin-Elmer Corporation: Minnesota, 1992, 233.
(61) Kumar, A.; Malhotra, L.; Chopra, K. A Study of Photostructural Changes in Amorphous P-Se Thin Films Using IR and X-Ray Photoelectron Spectroscopy. *J. Non-Cryst. Solids* **1989**, *107*, 212−218.
(62) Maragliano, C.; Lilliu, S.; Dahlem, M. S.; Chiesa, M.; Souier, T.; Stefancich, M. Quantifying Charge Carrier Concentration in ZnO Thin Films by Scanning Kelvin Probe Microscopy. *Sci. Rep.* **2014**, *4*, 4203.
(63) Kelvin, L. Contact Electricity of Metals. *London Edinb. Dublin Philos. Mag. J. Sci.* **1898**, *46*, 82−120.
(64) Mántica, A. M.; Detisch, M. J.; Balk, T. J. High-Temperature Contact Potential Difference Measurement of Surface Work Function Using in *vacuo* Kelvin Probe. *Vacuum* **2023**, *215*, 112169.
(65) Ho, C.-H.; Lee, H.-W.; Cheng, Z.-H. Practical Thermoreflectance Design for Optical Characterization of Layer Semiconductors. *Rev. Sci. Instrum.* **2004**, *75*, 1098−1102.
(66) Ho, C.-H.; Huang, Y.-S.; Tiong, K.-K.; Liao, P. C. Absorption-edge Anisotropy in ReS_2 and $ReSe_2$ Layered Semiconductors. *Phys. Rev. B* **1998**, *58*, 16130.
(67) Ho, C. H.; Hsu, T. Y.; Muhimmah, L. C. The Band-edge Excitons Observed in Few-layer $NiPS_3$. *npj 2D Mater. Appl.* **2021**, *5*, 8.
(68) Varshni, Y. P. Temperature Dependence of The Energy Gap in Semiconductors. *Physica* **1967**, *34*, 149−154.
(69) Pankove, J. I. *Optical Processes in Semiconductors*; Dover: New York, 1975.
(70) Ho, C. H.; Wang, Y. P.; Huang, Y. S. Optical Characterization of Band-edge Property of In_6S_7 Compound. *Appl. Phys. Lett.* **2012**, *100*, 131905.

https://doi.org/10.1021/jacsau.3c00653
JACS Au 2024, 4, 58−71